

Estimation of the Surface Heat Flux Response to Sea Surface Temperature Anomalies over the Global Oceans

SUNGSU PARK*

Advanced Study Program, National Center for Atmospheric Research, Boulder, Colorado

CLARA DESER

Climate and Global Dynamics Division, National Center for Atmospheric Research, Boulder, Colorado

MICHAEL A. ALEXANDER

NOAA-CIRES, University of Colorado, Boulder, Colorado

(Manuscript received 4 October 2004, in final form 21 February 2005)

ABSTRACT

The surface heat flux response to underlying sea surface temperature (SST) anomalies (the *surface heat flux feedback*) is estimated using 42 yr (1956–97) of ship-derived monthly turbulent heat fluxes and 17 yr (1984–2000) of satellite-derived monthly radiative fluxes over the global oceans for individual seasons. Net surface heat flux feedback is generally negative (i.e., a damping of the underlying SST anomalies) over the global oceans, although there is considerable geographical and seasonal variation. Over the North Pacific Ocean, net surface heat flux feedback is dominated by the turbulent flux component, with maximum values ($28 \text{ W m}^{-2} \text{ K}^{-1}$) in December–February and minimum values ($5 \text{ W m}^{-2} \text{ K}^{-1}$) in May–July. These seasonal variations are due to changes in the strength of the climatological mean surface wind speed and the degree to which the near-surface air temperature and humidity adjust to the underlying SST anomalies. Similar features are observed over the extratropical North Atlantic Ocean with maximum (minimum) feedback values of approximately $33 \text{ W m}^{-2} \text{ K}^{-1}$ ($9 \text{ W m}^{-2} \text{ K}^{-1}$) in December–February (June–August). Although the net surface heat flux feedback may be negative, individual components of the feedback can be positive depending on season and location. For example, over the midlatitude North Pacific Ocean during late spring to midsummer, the radiative flux feedback associated with marine boundary layer clouds and fog is positive, and results in a significant enhancement of the month-to-month persistence of SST anomalies, nearly doubling the SST anomaly decay time from 2.8 to 5.3 months in May–July.

Several regions are identified with net positive heat flux feedback: the tropical western North Atlantic Ocean during boreal winter, the Namibian stratocumulus deck off West Africa during boreal fall, and the Indian Ocean during boreal summer and fall. These positive feedbacks are mainly associated with the following atmospheric responses to positive SST anomalies: 1) reduced surface wind speed (positive turbulent heat flux feedback) over the tropical western North Atlantic and Indian Oceans, 2) reduced marine boundary layer stratocumulus cloud fraction (positive shortwave radiative flux feedback) over the Namibian stratocumulus deck, and 3) enhanced atmospheric water vapor (positive longwave radiative flux feedback) in the vicinity of the tropical deep convection region over the Indian Ocean that exceeds the negative shortwave radiative flux feedback associated with enhanced cloudiness.

* Current affiliation: Department of Atmospheric Sciences, University of Washington, Seattle, Washington.

Corresponding author address: Dr. Sungsu Park, Department of Atmospheric Sciences, University of Washington, Box 351640, Seattle, WA 98195-1640.
E-mail: sungsu@atmos.washington.edu

1. Introduction

Surface heat fluxes generate sea surface temperature (SST) anomalies, and SST anomalies, in turn, can modulate surface heat fluxes. Understanding how surface heat fluxes respond to underlying SST anomalies—*surface heat flux feedback*—is essential to understanding the nature of the coupled atmosphere–ocean sys-

tem. Physically, the surface heat flux feedback is expected to be strongly negative (i.e., damping the underlying SST anomalies) due to explicit enhancements of upward turbulent heat and longwave radiative fluxes over warm SST anomalies. However, atmospheric responses can either weaken or strengthen this explicit negative feedback. In general, moisture and temperature of the near-surface air increase over warm SST anomalies, resulting in a weakening of the negative turbulent feedback (e.g., the concept of reduced thermal damping; Barsugli and Battisti 1998). Further weakening of the negative feedback can occur in association with the following atmospheric responses to warm SST anomalies: reduced surface wind speed (positive turbulent flux feedback), reduced boundary layer cloud fraction (positive shortwave radiative feedback), and enhanced atmospheric water vapor (positive longwave radiative feedback). On the other hand, the negative feedback can be strengthened in association with enhanced surface wind speed or increased cirrus and stratiform clouds.

Conventionally, surface heat flux feedback has been estimated from the response of atmospheric general circulation models (GCMs) to prescribed SST anomalies (e.g., Frankignoul et al. 1998). However, as discussed by Frankignoul and Kestenare (2002, hereafter FK02), surface heat flux feedback can be different depending on the origins of the SST anomalies, requiring the use of the coupled ocean–atmospheric GCM simulations for reliable feedback estimation. Because simulated surface heat flux feedback differs between GCMs (Frankignoul et al. 2004), however, the surface heat flux feedback in nature should be estimated from observations. The problem is how to separate surface heat flux feedback and atmospheric forcing (independent of surface heat flux feedback) solely from the observed surface flux data.

Frankignoul et al. (1998) and FK02 suggested a method to estimate surface heat flux feedback over the North Pacific and Atlantic Oceans using observed monthly anomalies of SST and surface heat fluxes. After filtering out remote ENSO influences, FK02 decomposed the downwelling surface heat flux anomaly (Q') into the sum of a stochastic atmospheric forcing and oceanic feedback term ($-\lambda \cdot T'$, where λ is a constant feedback factor in watts per meters squared per kelvin and T' is the underlying SST anomaly). Given that the SST anomaly is essentially uncorrelated with stochastic atmospheric forcing at lags longer than the atmospheric persistence time scale (~ 1 – 2 weeks), feedback strengths of individual surface heat flux components were estimated as

$$\lambda(0) \equiv -\frac{\partial Q'}{\partial T'}(0) = -\frac{\text{Cov}[T'(-1), Q'(0)]}{\text{Cov}[T'(-1), T'(0)]}, \quad (1)$$

where Cov is covariance, (-1) and (0) are the values at the previous and present month, and a prime denotes the monthly anomaly. FK02 found that observed surface heat flux feedbacks are negative (positive λ) over the North Pacific and most of the Atlantic Oceans and are dominated by the turbulent heat flux feedback.

However, significant uncertainties exist in FK02's estimation of radiative heat flux feedback. In FK02, the net downwelling shortwave (SW) and longwave (LW) radiation at the sea surface were estimated using the conversion formulas of Reed (1977) and Budyko (1974) using the Comprehensive Ocean Atmosphere Data Set (COADS; Woodruff et al. 1987). However, these two conversion formulas greatly simplified spatial and temporal variations of clear sky and cloud optical properties, with the total cloud fraction as the only cloud variable explicitly considered. Recently, Zhang and Rossow (2004) calculated net downwelling SW and LW radiation by combining the International Satellite Cloud Climatology Project (ISCCP; Rossow and Schiffer 1991) satellite-derived cloud optical properties, observed clear-sky properties, and a radiative transfer model during July 1983–December 2000. This method explicitly incorporates spatial and temporal variations of clear-sky and cloud optical properties and is likely to be less affected by random observational error and sampling noise than the COADS ship observations.

In this study, we estimate radiative feedback using the ISCCP satellite-derived radiative flux data, unlike FK02 who used indirect estimates based on COADS cloud cover and empirical formulas. In addition, we examine the relative contributions of SW and LW radiation to net radiative feedback and each SW and LW feedback is further decomposed into the contributions of clear- and cloudy-sky radiation. Turbulent heat flux feedback is also analyzed in more detail than in FK02 by decomposing it into the contributions of moisture, temperature, and wind speed adjustments of the near-surface air to underlying SST anomalies.

A description of the data and analysis methods are given in section 2. In section 3, we discuss estimated turbulent (section 3a), radiative (section 3b), and net surface heat flux feedbacks (section 3c) including a comparison of the ship-derived and satellite-derived radiative fluxes (section 3b) and the role of surface heat flux feedback in the month-to-month persistence of the SST anomalies (section 3c). A summary and discussion are given in section 4.

2. Data and analysis methods

We follow the analysis methods employed by FK02. However, instead of using monthly data, individual ship observations are used to calculate surface heat fluxes. Using individual ship observations obtained from the Extended Edited Cloud Report Archive (EECRA; Hahn and Warren 1999), we constructed 5° latitude \times 10° longitude (also 5° latitude \times 5° longitude for Figs. 4 and 5) monthly data of SST, latent and sensible heat fluxes, net downwelling SW and LW fluxes at the sea surface during 1956–97. Latent and sensible heat fluxes are calculated from the bulk formulas using the transfer coefficients suggested by Isemer and Hasse (1985) and net downwelling SW and LW radiation at the sea surface are calculated from the formulas suggested by Reed (1977) and Budyko (1974), respectively. Ship-derived radiation data are used only for comparison with those of satellite products (e.g., Figs. 4 and 5) on which our estimation of radiative feedback is based. Details of bulk and conversion formulas used in this study are summarized in the appendix.

To reduce the effects of random observational error and sampling noise in the ship observations, a minimum of 20 observations per month were required in each monthly 5° latitude \times 10° longitude grid box; grids not satisfying this criteria were given missing values. Then, monthly climatologies were calculated requiring a minimum of 30 yr for each month in the 42-yr record and monthly anomalies were subsequently calculated. Missing values were filled by spatiotemporal interpolations using the nearby nonmissing grid values and then the data were detrended using a third-order polynomial. To minimize interpolation effects, only the grids with a minimum of 30 yr of nonmissing monthly values for each month before interpolations in the 42-yr record were used for the subsequent analysis. The fraction of missing values filled by the interpolations (mainly concentrated in the tropical Pacific, Indian, and South Atlantic Oceans) is about 5%. As a check, we repeated the same feedback estimates 1) by filling the missing gaps using empirical orthogonal functions (EOFs) instead of spatiotemporal interpolations, and 2) without filling the missing gaps. Both methods produced results similar to the ones shown here.

To use Eq. (1) to obtain unbiased feedback estimates, any low-frequency variations in the atmospheric forcing with decorrelation times longer than a month should be removed prior to the analysis. One source of low-frequency atmospheric variations is ENSO, which influences the global atmosphere and oceans via atmospheric teleconnections throughout the year (Lau and Nath 1996; Klein et al. 1999; Alexander et al. 2002,

2004; Park and Leovy 2004; Park 2004). The seasonally dependent ENSO influence was removed from the surface heat flux estimates as follows. First, ENSO indices were obtained from a covariance-based EOF analysis of monthly SST anomalies over the tropical Pacific and Indian Oceans between 20°N and 20°S using the “Kaplan” dataset (Kaplan et al. 1998) during January 1900–December 2002. The first three principal components (PCs), which explain 44.5%, 11.6%, and 7.3% of total variance, respectively, and are well separated from the other modes by the criteria of North et al. (1982), were used to remove the ENSO signal from the surface heat flux and SST by subtracting the simultaneous regression values of the monthly anomalies on the PC time series using three consecutive monthly values centered on each calendar month. This ENSO filtering was applied to the global ocean areas including tropical Pacific and Indian Oceans.

As a last step, in order to further reduce random observational error and sampling noise, we reconstructed monthly anomalies of SST and surface heat fluxes over the North Pacific, Atlantic, and tropical Pacific and Indian Oceans, respectively, by combining the EOF modes explaining 90% of the remaining ENSO-filtered variance in each domain.

In addition to ship observations, we analyzed monthly 5° latitude \times 10° longitude net and clear-sky downwelling SW and LW radiation data from ISCCP during January 1984–December 2000 (Zhang and Rossow 2004). Similar to the ship observations, we filtered out linear trends and ENSO signals but did not perform the EOF reconstruction because the satellite data are likely to be less affected by random observational error and sampling noise than are the ship observations. The 17-yr record of radiative fluxes may not be long enough to obtain statistically stable estimates of radiative feedback. However, it is expected that random observational error and sampling noise in the ISCCP-derived radiative heat flux data are much smaller than the ship derivations, compensating somewhat for the disadvantage of the short period of record.

To increase the number of realizations and thus reduce sampling noise, seasonal values of the damping coefficient λ are estimated using three consecutive monthly anomalies following the methodology of FK02. For example, λ during June–August (JJA) is estimated by correlating *monthly* heat flux anomalies in JJA with *monthly* SST anomalies in May, June, and July:

$$\lambda(\text{JJA}) = - \frac{\text{Cov} \left[\begin{array}{c} \text{SST}'(\text{May, Jun, Jul}), \\ Q'(\text{Jun, Jul, Aug}) \end{array} \right]}{\text{Cov} \left[\begin{array}{c} \text{SST}'(\text{May, Jun, Jul}), \\ \text{SST}'(\text{Jun, Jul, Aug}) \end{array} \right]}.$$

TABLE 1a. Average heat flux feedback parameters over the North Pacific Ocean. Area mean values (area-weighted averages of individual $5^\circ \text{ lat} \times 10^\circ \text{ lon}$ grid boxes) of seasonal heat flux parameters for the North Pacific Ocean ($25^\circ\text{--}55^\circ\text{N}$, $140^\circ\text{E}\text{--}120^\circ\text{W}$). Values in parentheses are monthly climatologies of SST $- T_a$ (K), RH [relative humidity of near-surface air (%)], and U (m s^{-1}). Units of $\lambda_{(q_s-q_v)}$ [Eq. (2)], $\lambda_{(\text{SST}-T_a)}$ [Eq. (2)], λ_{RH} , and λ_U [Eq. (3)] are $\text{g kg}^{-1} \text{ K}^{-1}$, K K^{-1} , $\% \text{ K}^{-1}$, and $\text{m s}^{-1} \text{ K}^{-1}$, respectively, and $\lambda_a \equiv \lambda_{\text{LHF}} + \lambda_{\text{SHF}} + \lambda_{\text{SW}} + \lambda_{\text{LW}}$. The units of the last two rows in Tables 1a,b are month and the others have units of $\text{W m}^{-2} \text{ K}^{-1}$. Turbulent, radiative, and net feedback parameters are signified by bold characters.

	Jan	Feb	Mar	Apr	May	Jun	Jul	Aug	Sep	Oct	Nov	Dec	Yr
$\overline{\lambda_{\text{LHF}} + \lambda_{\text{SHF}}}$	27.0	23.9	23.3	15.9	11.4	9.0	10.2	12.1	15.6	18.7	21.8	22.9	19.1
λ_{OT}	22.4	19.4	17.9	12.5	9.6	8.5	9.7	10.8	13.3	15.7	19.2	19.8	16.0
λ_{WS}	3.1	2.8	3.2	1.7	0.8	0.5	0.3	0.6	1.5	2.4	2.1	1.8	1.6
$-\lambda_{(q_s-q_v)}$	0.39	0.37	0.38	0.31	0.29	0.30	0.37	0.40	0.41	0.39	0.40	0.37	0.41
$-\lambda_{(\text{SST}-T_a)}$	0.29	0.25	0.26	0.19	0.14	0.12	0.14	0.16	0.19	0.20	0.24	0.24	0.22
	(1.9)	(1.6)	(1.1)	(0.5)	(-0.1)	(-0.3)	(-0.3)	(-0.1)	(0.4)	(0.9)	(1.5)	(1.8)	(0.7)
$-\lambda_{\text{RH}}$	-1.1	-1.1	-1.2	-1.0	-0.9	-0.8	-1.0	-0.9	-0.8	-0.7	-0.9	-0.9	-1.2
	(79.5)	(79.5)	(79.5)	(80.1)	(82.2)	(84.3)	(85.0)	(84.0)	(81.5)	(79.8)	(78.8)	(79.0)	(81.1)
$-\lambda_U$	0.15	0.17	0.24	0.19	0.14	0.10	0.10	0.11	0.17	0.17	0.13	0.07	0.15
	(10.3)	(10.0)	(9.4)	(8.5)	(7.6)	(6.9)	(6.5)	(6.6)	(7.4)	(8.5)	(9.5)	(10.1)	(8.4)
$\overline{\lambda_{\text{SW}}} + \lambda_{\text{LW}}$	1.0	0.6	0.7	-2.5	-3.9	-4.3	-2.5	-2.2	-2.6	-2.4	-1.1	-0.1	-2.4
$\overline{\lambda_{\text{SW}}}$	-0.6	-0.5	-0.7	-3.7	-6.6	-6.8	-5.9	-4.7	-4.2	-2.7	-1.5	-0.8	-3.8
$\overline{\lambda_{\text{SW,cloud}}}$	-0.8	-0.6	-0.8	-3.9	-6.8	-7.1	-6.3	-5.2	-4.7	-2.9	-1.5	-0.9	-4.2
$\overline{\lambda_{\text{LW}}}$	1.6	1.0	1.3	1.2	2.6	2.5	3.3	2.5	1.7	0.3	0.4	0.7	1.4
$\overline{\lambda_{\text{LW,clear}}}$	1.3	0.7	1.4	1.3	1.1	0.7	1.6	0.8	-0.2	-1.2	-0.6	0.0	0.1
λ_a	28.0	24.5	24.0	13.4	7.5	4.7	7.7	9.9	13.0	16.3	20.7	22.8	16.7
$\left(\frac{\overline{\lambda_{\text{LHF}} + \lambda_{\text{SHF}}}}{\rho \cdot C_p \cdot H}\right)^{-1}$	5.4	6.3	5.1	5.2	3.6	2.8	2.0	1.8	2.1	2.5	2.8	4.3	3.7
$\left(\frac{\overline{\lambda_a}}{\rho \cdot C_p \cdot H}\right)^{-1}$	5.1	6.1	4.8	6.1	5.1	5.3	2.9	2.3	2.6	2.9	3.0	4.2	4.4

Area mean values of seasonal and annual heat flux feedback parameters are summarized in Tables 1a–c for several geographical domains. For the estimation of the annual feedback parameters in these tables, we first calculated λ s for three different lags of 1, 2, and 3

months using all 12 monthly values in the above equation, and the annual λ was obtained by averaging the three λ s.

Although the ENSO signals were removed, our feedback estimation over the tropical Pacific and Indian

TABLE 1b. Same as in Table 1a but for the extratropical North Atlantic Ocean ($20^\circ\text{--}60^\circ\text{N}$, $80^\circ\text{W}\text{--}0^\circ$).

	Jan	Feb	Mar	Apr	May	Jun	Jul	Aug	Sep	Oct	Nov	Dec	Yr
$\overline{\lambda_{\text{LHF}} + \lambda_{\text{SHF}}}$	29.5	26.5	18.1	17.2	15.7	14.8	12.2	15.1	19.1	23.7	25.8	29.0	22.3
λ_{OT}	22.6	20.5	14.9	13.2	11.8	12.1	11.0	12.7	14.7	18.5	20.6	22.7	17.1
λ_{WS}	4.6	3.9	1.9	2.2	1.7	0.9	0.0	1.0	2.3	3.6	3.7	4.4	2.0
$-\lambda_{(q_s-q_v)}$	0.46	0.44	0.37	0.38	0.42	0.49	0.46	0.52	0.52	0.56	0.50	0.48	0.49
$-\lambda_{(\text{SST}-T_a)}$	0.30	0.27	0.19	0.17	0.15	0.15	0.13	0.14	0.17	0.20	0.25	0.28	0.22
	(1.7)	(1.5)	(1.0)	(0.6)	(0.1)	(-0.1)	(-0.1)	(0.1)	(0.5)	(1.0)	(1.4)	(1.7)	(0.8)
$-\lambda_{\text{RH}}$	-0.7	-0.8	-0.7	-0.9	-1.1	-1.4	-1.0	-1.1	-1.1	-1.3	-0.9	-0.7	-1.0
	(77.4)	(77.4)	(77.8)	(78.1)	(79.7)	(81.4)	(81.7)	(80.9)	(79.7)	(78.4)	(77.3)	(77.2)	(78.9)
$-\lambda_U$	0.28	0.24	0.12	0.15	0.13	0.11	0.03	0.10	0.16	0.25	0.24	0.27	0.17
	(9.0)	(8.9)	(8.5)	(7.6)	(6.8)	(6.3)	(6.2)	(6.6)	(7.4)	(8.2)	(8.2)	(8.9)	(7.6)
$\overline{\lambda_{\text{SW}}} + \lambda_{\text{LW}}$	3.4	2.4	2.3	-1.0	-1.8	-2.8	-2.8	-0.8	-0.1	1.8	1.5	1.8	1.1
$\overline{\lambda_{\text{SW}}}$	1.3	-0.2	1.6	-0.2	-1.1	-3.6	-4.3	-1.6	0.1	1.6	1.0	0.2	-0.1
$\overline{\lambda_{\text{SW,cloud}}}$	1.8	0.3	2.2	0.4	-0.5	-2.9	-3.6	-0.9	1.0	2.8	2.3	1.1	0.9
$\overline{\lambda_{\text{LW}}}$	2.1	2.6	0.7	-0.9	-0.7	0.8	1.5	0.8	-0.2	0.2	0.5	1.6	1.2
$\overline{\lambda_{\text{LW,clear}}}$	3.3	3.2	1.6	-1.3	-1.6	-1.6	-0.8	-0.7	-0.2	0.7	1.5	2.1	1.7
λ_a	32.9	28.9	20.4	16.2	13.9	12.0	9.4	14.3	19.0	25.5	27.3	30.8	23.3
$\left(\frac{\overline{\lambda_{\text{LHF}} + \lambda_{\text{SHF}}}}{\rho \cdot C_p \cdot H}\right)^{-1}$	5.1	6.2	7.6	4.6	2.3	1.4	1.4	1.4	1.8	2.2	2.9	3.9	3.4
$\left(\frac{\overline{\lambda_a}}{\rho \cdot C_p \cdot H}\right)^{-1}$	4.4	5.3	6.4	5.0	2.8	1.9	1.7	1.5	1.9	2.1	2.8	3.6	3.3

TABLE 1c. Same as in Table 1a but for the tropical Atlantic Ocean (20°S–20°N, 80°W–10°E).

	Jan	Feb	Mar	Apr	May	Jun	Jul	Aug	Sep	Oct	Nov	Dec	Yr
$\overline{\lambda_{LHF} + \lambda_{SHF}}$	3.4	3.7	3.5	2.8	3.7	6.4	7.2	9.1	8.4	10.6	7.3	5.6	6.5
λ_{OT}	9.6	9.6	8.9	7.7	8.3	7.9	8.6	8.2	8.9	11.4	11.0	10.7	8.9
λ_{WS}	-5.7	-5.4	-5.2	-4.3	-3.8	-1.7	-2.4	-0.2	-1.0	-1.2	-3.5	-4.6	-2.5
$-\lambda_{(q_s-q_v)'}'$	0.40	0.41	0.39	0.33	0.33	0.30	0.33	0.32	0.36	0.46	0.43	0.42	0.35
$-\lambda_{(SST-T_d)'}'$	0.10	0.09	0.10	0.09	0.09	0.07	0.07	0.05	0.06	0.10	0.11	0.11	0.08
$-\lambda_{RH'}$	-0.1	-0.2	0.1	0.3	0.3	0.1	0.1	-0.1	-0.1	-0.5	-0.2	-0.2	0.1
$-\lambda_{U'}$	-0.31	-0.30	-0.28	-0.23	-0.21	-0.10	-0.12	0.00	-0.05	-0.06	-0.18	-0.24	-0.14
	(6.3)	(6.2)	(6.1)	(6.2)	(6.3)	(6.5)	(6.4)	(6.3)	(6.1)	(6.0)	(6.1)	(6.2)	(6.2)
$\overline{\lambda_{SW} + \lambda_{LW}}$	-1.4	1.8	-0.1	-1.2	0.0	-1.0	0.2	-2.0	-2.7	-6.1	-7.2	-5.1	1.1
$\overline{\lambda_{SW}}$	-1.0	1.8	-0.4	-0.9	-1.6	-3.9	-3.2	-5.2	-5.9	-10.4	-9.6	-5.8	-2.7
$\overline{\lambda_{SW,cloud}}$	0.3	2.7	1.1	0.5	-0.4	-2.4	-1.2	-2.1	-1.8	-5.4	-5.5	-3.1	0.1
$\overline{\lambda_{LW}}$	-0.5	0.0	0.3	-0.2	1.6	2.9	3.4	3.2	3.3	4.2	2.4	0.7	3.8
$\overline{\lambda_{LW,clear}}$	-2.4	-1.3	-1.2	-2.3	-0.7	0.3	1.3	0.0	-0.9	-0.7	-2.0	-2.5	1.3
$\overline{\lambda_d}$	2.0	5.5	3.4	1.6	3.7	5.5	7.4	7.1	5.7	4.5	0.1	0.5	7.6

Oceans may still be biased due to the potential persistence of the atmospheric forcing in the remaining dynamic coupling variation modes between the atmosphere and ocean. In addition, over the regions where ENSO effects dominate the total variances, the remaining covariances between the ENSO-filtered SST and surface fluxes may be too weak to produce reliable feedback estimates. Thus, only qualitative interpretations of the results are valid in these regions.

3. Results

a. Turbulent heat flux feedback

Figure 1 shows estimated turbulent heat flux feedback for the four seasons. Domains used for the EOF reconstructions (North Pacific, Atlantic, and tropical Pacific and Indian Oceans) are indicated by thick black lines. If the SST autocorrelation at 1-month lag does not differ from zero at the 95% confidence level from

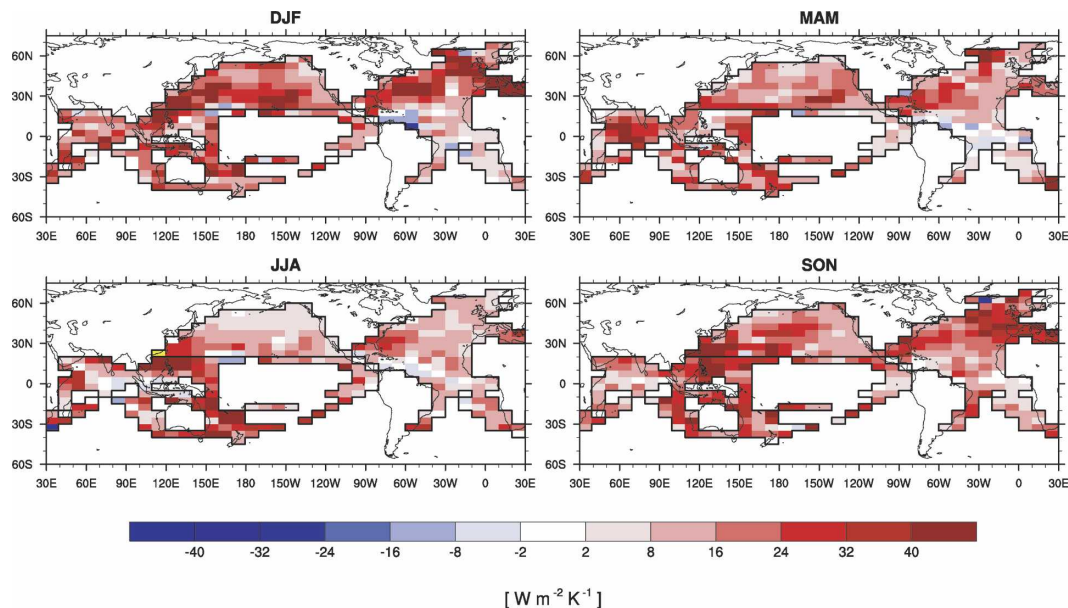


FIG. 1. Turbulent heat flux feedback ($\lambda_{LHF} + \lambda_{SHF}$, the sum of latent and sensible heat flux feedbacks) for each season estimated from the EECRA ship observation. The EOF reconstruction domains for the North Pacific, Atlantic, and tropical Pacific and Indian Oceans are indicated by thick black lines. Grids where SST autocorrelation at 1-month lag does not differ from zero at the 95% confidence level from the two-sided Student's t test assuming independent samples (e.g., the East China Sea, west of Taiwan in JJA) are indicated by yellow shading.

the two-sided Student's t test assuming independent samples, λ was not estimated (indicated by yellow shading in the figures).

Over the North Pacific and extratropical North Atlantic Oceans, turbulent heat flux feedback damps SST anomalies (positive λ) in all seasons, with maximum (minimum) values during winter (summer). During December–February (DJF), regions of strong negative turbulent heat flux feedback with magnitudes over $40 \text{ W m}^{-2} \text{ K}^{-1}$ occur over the far western subtropical North Pacific, central North Pacific (north of the Hawaiian Islands), central and northeastern Atlantic, and the Mediterranean Sea. Over the tropical Atlantic Ocean, turbulent heat flux feedback is generally weaker than the North Pacific and extratropical North Atlantic Oceans. Regions of positive turbulent heat flux feedback (negative λ) occur over the western tropical Atlantic during DJF and over the central tropical Atlantic during March–May (MAM). Over the tropical Pacific and Indian Oceans, turbulent heat flux feedback generally damps SST anomalies. Over the Indian Ocean, negative turbulent heat flux feedback is strongest during the boreal spring but weak during the boreal fall while a reverse pattern is observed over the western tropical Pacific Ocean. In general, except in the tropical Pacific and Indian Oceans, overall patterns and magnitudes of estimated turbulent heat flux feedback are similar to FK02.

To obtain insights into the mechanisms responsible for the observed turbulent heat flux feedback, we repeated the same lag-covariance analysis using $(q_s - q_v)'$ [q_s : saturation specific humidity at SST with a correction of salinity effect (see the appendix), q_v : specific humidity of surface air], $(\text{SST} - T_a)'$ (T_a : surface air temperature), and surface scalar wind speed anomaly (U'). After calculating λ for each $(q_s - q_v)'$, $(\text{SST} - T_a)'$, and U' from Eq. (1) (note that the units of λ for this case is not watts per meters squared per kelvin but grams per kilograms per kelvin, kelvins per kelvin, and meters per second per kelvin, respectively), independent contributions of moisture–temperature adjustment and wind speed adjustment to turbulent heat flux feedback were estimated as

$$\lambda_{\text{QT}} = [L_v \overline{\rho C_q} \lambda_{(q_s - q_v)'} + C_p \overline{\rho C_h} \lambda_{(\text{SST} - T_a)'}] \overline{U}, \quad (2)$$

$$\lambda_{\text{WS}} = [L_v \overline{\rho C_q} (\overline{q_s} - \overline{q_v}) + C_p \overline{\rho C_h} (\overline{\text{SST}} - \overline{T_a})] \lambda_{U'}, \quad (3)$$

where the overbar denotes the monthly climatology at each grid point, λ_{QT} and λ_{WS} are the turbulent heat flux feedbacks associated with moisture–temperature and wind speed adjustments of near-surface air, respec-

tively, and definitions of the other variables are in the appendix. Note that λ_{WS} represents a *dynamics feedback* that was not considered in the classical Hasselmann-type stochastic model (Frankignoul 1985). Although C_q and C_h are functions of $\text{SST} - T_a$ and U and the contribution of $\lambda_{(q_s - q_v)'(\text{SST} - T_a)'}$ is neglected, the sum of λ_{QT} and λ_{WS} roughly corresponds to turbulent heat flux feedback (not shown but see Tables 1a–c).

Figure 2 shows the turbulent heat flux feedback associated with moisture–temperature adjustment of the near-surface air, λ_{QT} [Eq. (2)]. Comparison of Fig. 2 with Fig. 1 indicates that over the extratropical oceans, strong negative turbulent heat flux feedback (highly positive λ) stems mainly from relatively weak moisture–temperature adjustment of near-surface air to underlying SST anomalies. In these regions, annual cycles of turbulent heat flux feedback are largely explained by the annual cycles of λ_{QT} , about half of which is from the annual cycle of moisture–temperature adjustment, $\lambda_{\text{QT}}/\overline{U}$, and the remaining is from the annual cycle of climatological surface wind, \overline{U} (Tables 1a,b). Note that over the extratropical oceans, relative humidity of the near-surface air generally decreases over warm SST anomalies ($\sim -1\% \text{ K}^{-1}$; Tables 1a,b), implying that cloud-base height (i.e., lifting condensation level) rises as SST increases.

Figure 3 shows the turbulent heat flux feedback associated with the wind speed adjustment of near-surface air, λ_{WS} [Eq. (3)]. The contribution of λ_{WS} to turbulent heat flux feedback is generally weaker than λ_{QT} especially over the extratropical oceans but λ_{WS} shows nontrivial temporal and spatial variations with significant sign reversals. In particular, positive turbulent heat flux feedback over the western and central tropical Atlantic Ocean in Fig. 1 are due to reduced surface wind speeds over warmer SST anomalies. This feature, often referred to as “wind–evaporation–SST feedback,” has been interpreted as the results of the variations of climatological Atlantic trade winds in responses to regional SST anomalies: hydrostatic reduction of local sea level pressure (SLP) over warm SST anomalies induces anomalous cross-equatorial pressure gradient forces, which results in the weakening of local trade wind speed over warm SST anomalies (e.g., Chang et al. 2001). Because this region is strongly influenced by tropical Pacific SST anomalies (Alexander and Scott 2002; Wang and Enfield 2003), which can reinforce positive heat flux feedback in this region (Saravanan and Chang 2000), parts of observed positive feedback may be associated with the imperfect removal of *nonlinear* remote ENSO influences (Hoerling et al. 1997).

Reduction of surface wind speed over warm SST

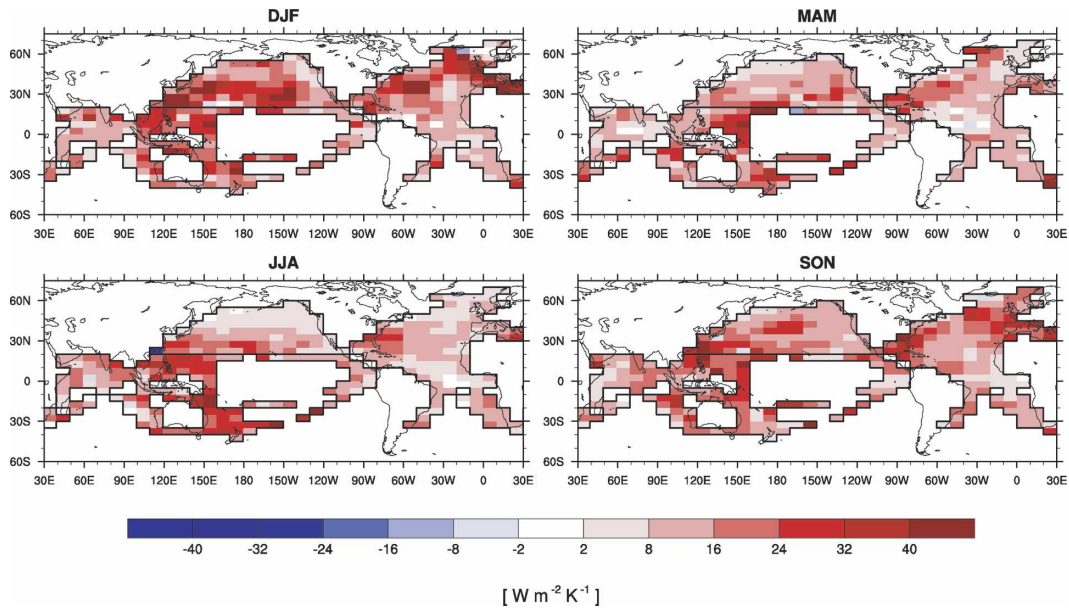


FIG. 2. Same as in Fig. 1 but for turbulent heat flux feedback in association with moisture–temperature adjustment of near-surface air to underlying SST anomalies estimated from EECRA ship observations [λ_{OT} in Eq. (2)].

anomalies also occurs over the equatorial Indian Ocean in September–November (SON) contrasting to the enhanced surface wind speed in MAM. Similar features with opposite polarities are also observed over the western tropical Pacific Ocean. Note that this wind speed adjustment significantly contributes to the annual cycle of turbulent heat flux feedback in these tropical

regions (see Fig. 1 and Table 1c) in contrast to midlatitude areas where the annual cycle of moisture–temperature adjustment is the dominant contributor.

Regions of strong negative turbulent heat flux feedback (highly positive λ) over the North Pacific and extratropical North Atlantic Oceans in autumn and winter (Fig. 1) are in part associated with enhanced surface

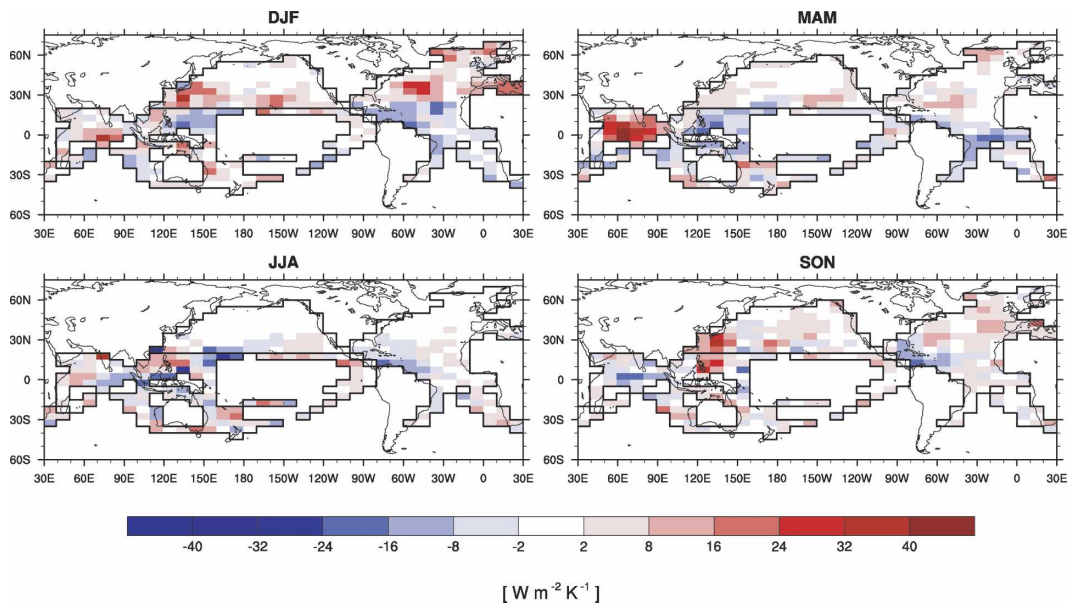


FIG. 3. Same as in Fig. 1 but for turbulent heat flux feedback in association with wind speed adjustment of near-surface air to underlying SST anomalies estimated from EECRA ship observations [λ_{WS} in Eq. (3)].

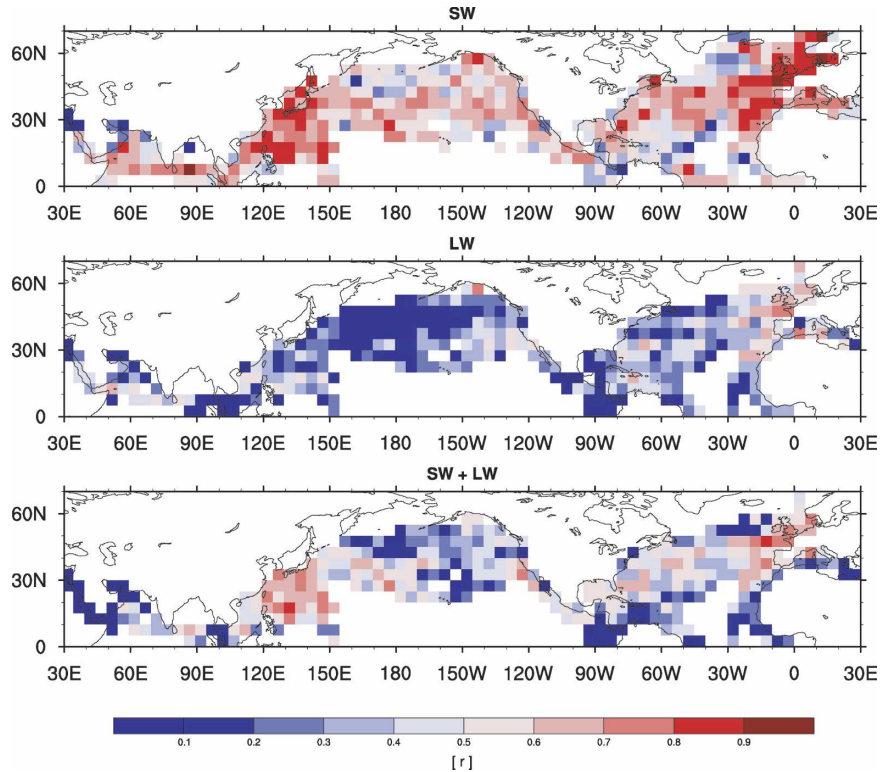


FIG. 4. Interannual correlation coefficients between ISCCP satellite-derived and EECRA ship-derived net downwelling (a) SW, (b) LW, and (c) SW + LW radiation during JJA based on the period 1984–97.

wind speed over warm SST anomalies (Fig. 3). Using satellite data, Nonaka and Xie (2003) found a similar increase of surface wind speeds over warm SST anomalies over the Kuroshio and its extension. Over the North Pacific and extratropical North Atlantic, maximum λ_{OT} roughly coincides with maximum λ_{WS} . In these areas, the adjustments of T'_a and q'_v are weak and relative humidity of surface air shows strong reduction (up to $-3\% \text{ K}^{-1}$) over warm SST anomalies (not shown). This implies that cooling and drying processes tend to counteract the surface flux forcing. As discussed by Nonaka and Xie (2003), this is likely to reflect enhanced incorporation of dry and fast-moving upper air into the marine boundary layer (MBL) due to enhanced strength of boundary layer turbulence over warm SST anomalies. However, it is not clear how this mechanism alone can induce cooling anomalies of near-surface air given a statistically stable layer across the top of atmospheric MBL. It is speculated that nonlocal or diabatic processes involving atmospheric circulation changes may play roles here.

b. Radiative heat flux feedback

In this section, we first compare ship- and satellite-derived radiation fields to show that radiative feed-

backs estimated from the two different datasets can be significantly different. Then, radiative feedback estimated from the satellite derivation will be discussed in detail in each geographical domains.

Figure 4 shows interannual correlation coefficients between satellite- and ship-derived net downwelling SW, LW, and SW + LW radiation at the sea surface during JJA. SW radiation from Reed's formula is well correlated with those from ISCCP over the northeastern Atlantic and subtropical western Pacific Oceans (correlation coefficient, $r = 0.7\sim 0.9$). In contrast, LW radiation is essentially uncorrelated in the two datasets over most of the global ocean except the far northeastern Atlantic Ocean. The resulting net radiation shows relatively high correlations over the northeastern Atlantic and subtropical western North Pacific Oceans but over most of the remaining ocean areas, correlations are very weak. Figure 5 shows a function of the ratio of the interannual standard deviations during JJA derived from ship versus satellite estimates. Not only weakly correlated, they also show systematic differences in the magnitude of variance. Significantly, the underestimated variances of LW radiation by Budyko's formula are $\sim 50\%$ – 100% of the ISCCP variances over most of the oceans. The same analysis during DJF shows that

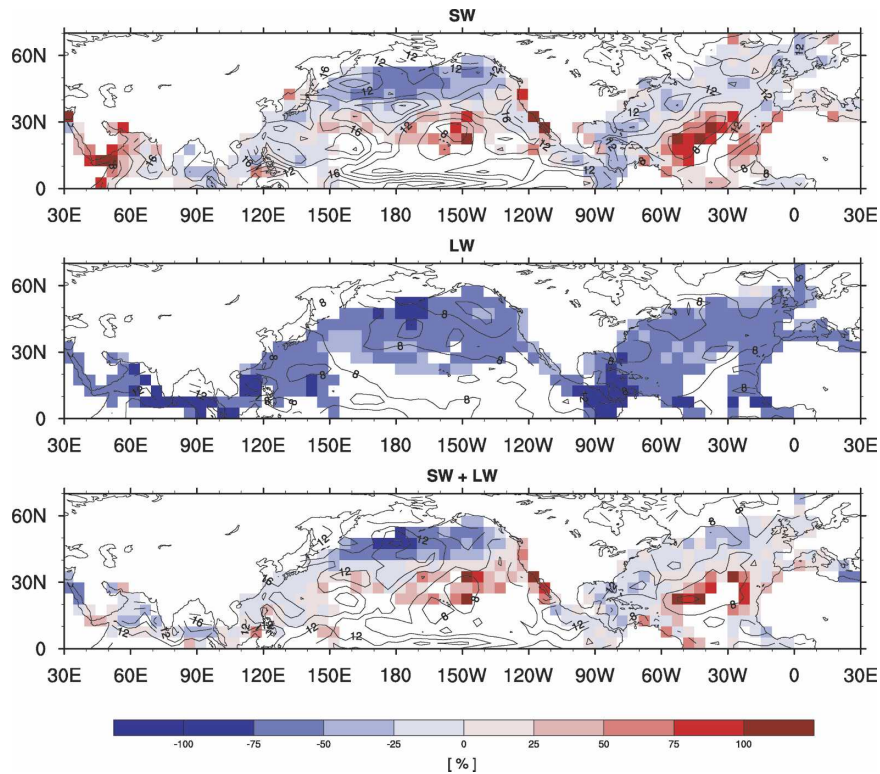


FIG. 5. Ratio of ship-derived to satellite-derived standard deviations of net downwelling (a) SW, (b) LW, and (c) SW + LW radiation, expressed as the fraction $[100 \cdot (\sigma_{\text{EECRA}}/\sigma_{\text{ISCCP}} - 1)]$, where σ is the interannual std dev during JJA. Red (blue) shading indicates that the ship- (satellite-) derived values are larger than those from satellites (ships). Climatologies of interannual standard deviations of ISCCP radiation during JJA are plotted as solid lines in each figure with a contour interval of 2 W m^{-2} .

over the midlatitude oceans, net radiation is less well correlated than in JJA even though differences of interannual standard deviations are reduced due partly to the weak incoming SW radiation at the top of the atmosphere during DJF (not shown). Both the weak correlations and difference in standard deviations are likely to result in different estimates of radiative flux feedback [Eq. (1)].

The sum of the SW and LW feedback estimated from the satellite observations is shown in Fig. 6, and the individual components in Fig. 7 (SW) and Fig. 8 (LW). To get insights into the mechanisms responsible for the observed radiative feedback, we also analyzed clear-sky radiative feedback using clear-sky radiation data at the sea surface. The cloud contribution to radiative feedback was estimated by subtracting clear-sky radiative feedback from the net sky radiative feedback. The results of clear-sky and cloud radiative feedbacks are shown in Fig. 9 (clear-sky SW) and in Figs. 10–11 (LW). As a whole, SW feedback is largely dominated by the cloud component, which is similar to Fig. 7. In contrast, LW feedback is mostly from the clear-sky component

but the contribution of cloud LW feedback is not negligible especially over regions where MBL stratocumulus clouds are abundant.

1) NORTH PACIFIC OCEAN

Over the North Pacific, radiative feedback is generally positive (negative λ) during midspring–fall but is negative (positive λ) during winter centered to the south of Alaska, with maximum values $\sim 8\text{--}16 \text{ W m}^{-2} \text{ K}^{-1}$ (Fig. 6 and Table 1a). During summer, regions of positive radiative feedback with magnitude $\sim 8\text{--}16 \text{ W m}^{-2} \text{ K}^{-1}$ occurs over the far western and eastern Pacific, and central North Pacific along the 37.5°N . During fall, positive radiative feedback weakens over the central North Pacific but strengthens over the eastern subtropical North Pacific west of California.

Over the eastern and central North Pacific, most of positive radiative feedback comes from strong positive SW feedback (slightly cancelled by weaker negative LW feedback) in association with MBL stratocumulus clouds that are highly reflective to SW radiation and have low cloud-top height (Fig. 7). Parts of positive SW

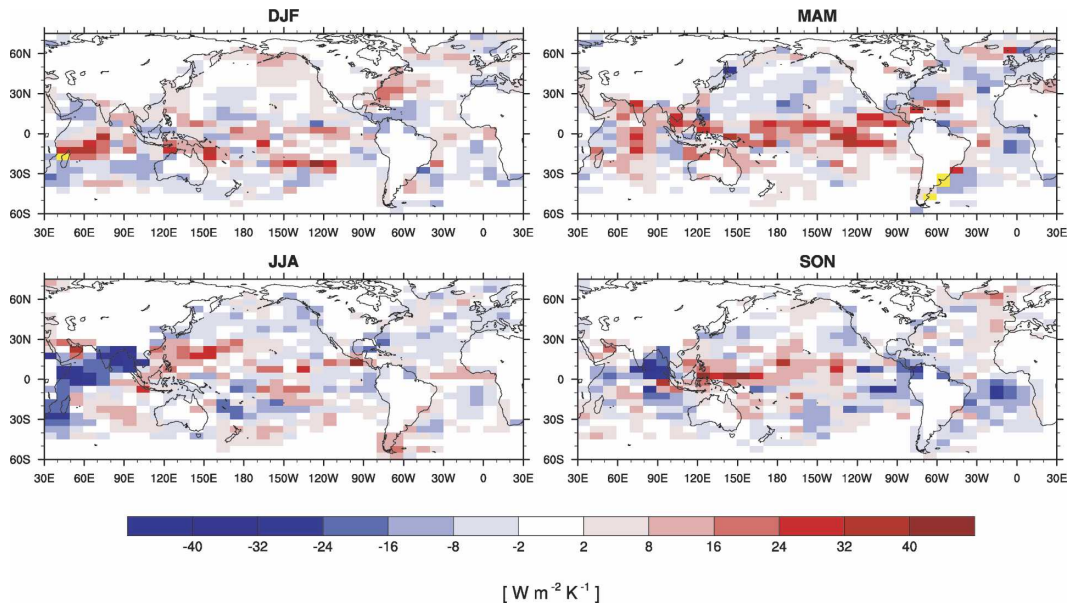


FIG. 6. Same as in Fig. 1 but for radiative heat flux feedback ($\lambda_{SW} + \lambda_{LW}$) estimated from ISCCP satellite data.

feedback over the western and central North Pacific north of $40^{\circ}N$ during summer are likely to be associated with the fog that is favored by colder water and stable atmospheric surface layer (see Table 1a) under northward advection (Norris 1998a,b). Magnitudes of cloud SW feedback in these regions are $6\text{--}20 W m^{-2} K^{-1}$ and can be up to $28 W m^{-2} K^{-1}$ over the California stra-

tocumulus deck during boreal fall. Because the variations of California stratocumulus clouds are strongly influenced by the variations of *upstream* boundary conditions in association with strong trade winds (Klein 1997; Park et al. 2004), Eq. (1) may underestimate this nonlocal feedback effect. Over the central North Pacific in JJA, strong positive SW feedback is distributed

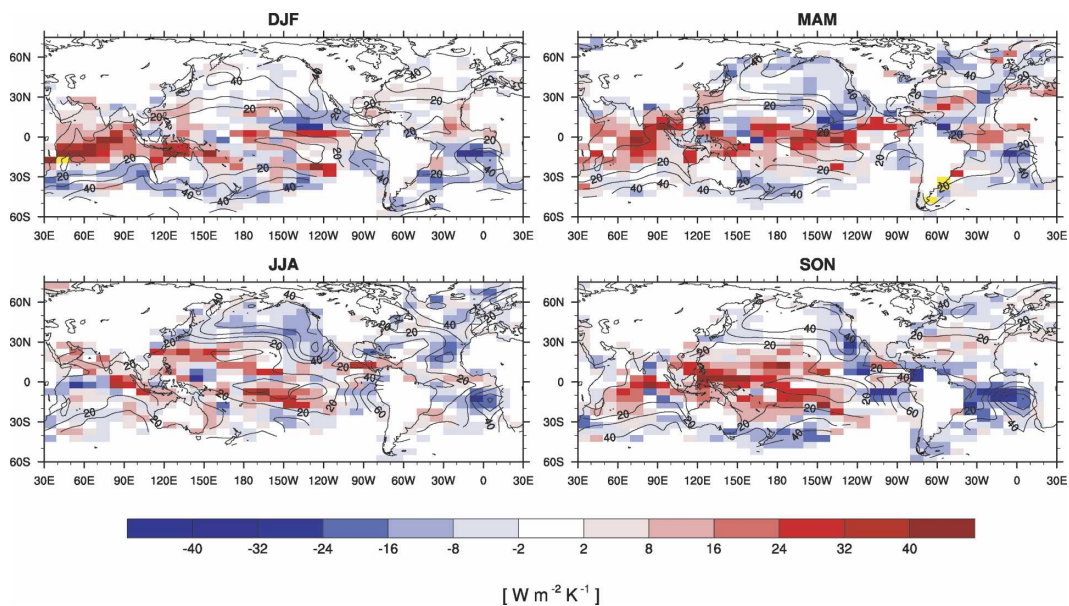


FIG. 7. Same as in Fig. 1 but for SW feedback (λ_{SW}) estimated from ISCCP satellite data. Solid lines in each figure are seasonal climatologies of stratocumulus plus fair-weather stratus amount obtained from EECRA ship observations during 1956–95.

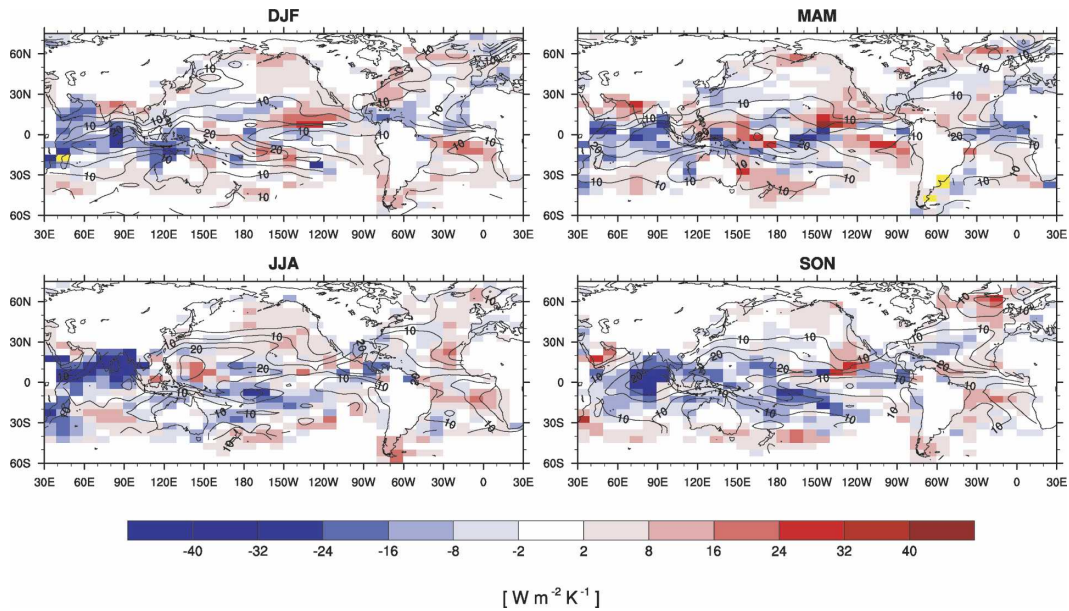


FIG. 8. Same as in Fig. 1 but for LW feedback (λ_{LW}) estimated from ISCCP satellite data. Solid lines in each figure are seasonal climatologies of cumulonimbus frequency obtained from EECRA ship observations during 1956–95.

along a zonal band where meridional gradients of climatological stratocumulus cloud fraction and SST are strongest. This is consistent with Norris (2000) who showed that a poleward shift of the SST gradient zone provides unfavorable conditions for stratocumulus formation, which in turn can strengthen the local warm SST anomalies. A similar analysis using ship-observed

stratocumulus cloud fraction indicates that strong SW feedback over the eastern and central North Pacific is largely associated with the variations of MBL stratocumulus cloud fraction [not shown but see Norris and Leovy (1994)]. Over the California stratocumulus deck, warm SST anomalies are likely to promote vertical deepening and decoupling of the MBL and so limit

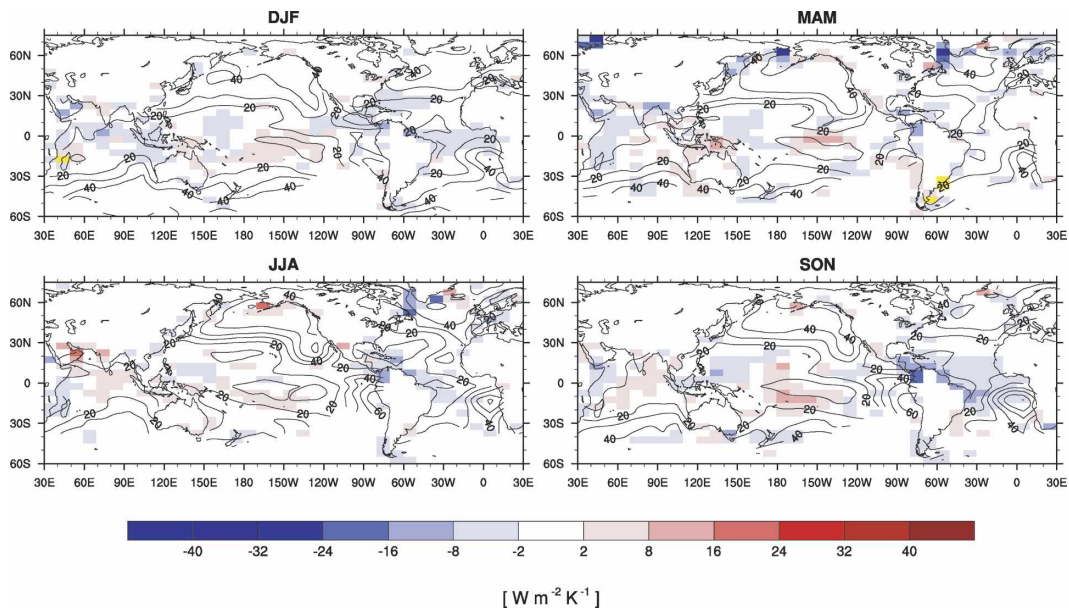


FIG. 9. Same as in Fig. 7 but for clear-sky SW feedback.

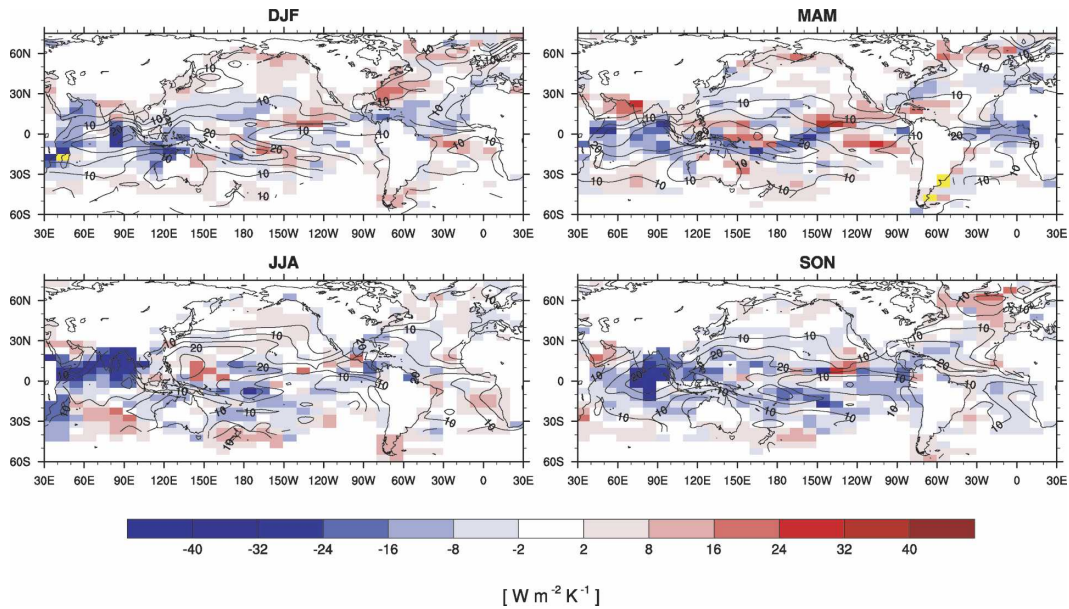


FIG. 10. Same as in Fig. 8 but for clear-sky LW feedback.

moisture transport from the sea surface to MBL stratocumulus clouds, resulting in the reduction of MBL cloud fraction (Bretherton and Wyant 1997; Park et al. 2004). Over the central North Pacific, weakened cold advection associated with reduced activity of synoptic storms over warm SST anomalies may further contribute to the reduction of stratocumulus cloud fraction (Norris 2000; Park and Leovy 2004).

Over the subtropical western North Pacific, modula-

tion of clear-sky LW radiation also contributes to the positive radiative feedback (Fig. 8). Similar but much stronger positive LW feedback is observed over the tropical Pacific and Indian Oceans where deep convection frequently occurs. It is speculated that positive LW feedback is partly associated with enhanced atmospheric water vapor over warm SST anomalies, which enhances downwelling LW radiation enough to compensate for enhanced upwelling LW radiation over

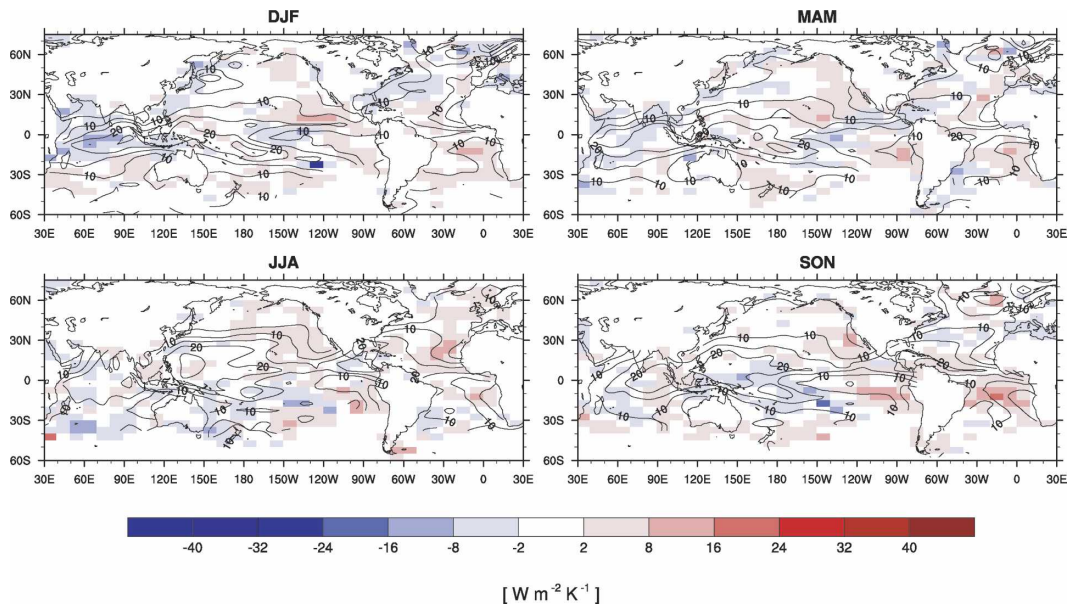


FIG. 11. Same as in Fig. 8 but for cloud LW feedback.

warmer SST anomalies (Manabe and Strickler 1964). Contrasting behavior is observed over the far northeastern Pacific south of Alaska during winter–spring, where mean SST and atmospheric water vapor are much lower than over the western subtropical North Pacific.

2) ATLANTIC OCEAN

Radiative feedback over the Atlantic Ocean shows complex seasonal and geographical variations. One of the most significant features is strong positive radiative feedback (negative λ) west of South Africa in the Namibian stratocumulus deck region. This positive feedback is especially large during SON with magnitudes up to $24\text{--}32 \text{ W m}^{-2} \text{ K}^{-1}$, strong enough to compensate for negative turbulent heat flux feedback in this region (Fig. 1). Note that maximum positive SW feedback tends to be located over the maximum gradient of stratocumulus cloud fraction on the equatorward flank of the stratocumulus deck (Fig. 7). Positive SW feedback associated with MBL stratocumulus clouds is also observed over the stratocumulus deck in the eastern subtropical North Atlantic Ocean during JJA and MAM. However, negative LW feedback significantly cancels the positive SW feedback especially during summer.

Except in MAM, positive LW feedback tends to occur over the western tropical and subtropical North Atlantic Ocean where deep convection frequently occurs. During MAM when the Atlantic ITCZ is well developed and at its southernmost position, positive LW feedback is also observed. This positive LW feedback is mainly associated with the variation of clear-sky radiation, suggesting that the increase of atmospheric water vapor over warmer SST anomalies is responsible. In contrast, SW feedback in the vicinity of these deep convection zones varies in a complex way depending on season and geographical location. The resulting net radiative feedback is positive over the Caribbean Sea and northern coast of South America during SON and DJF. In combination with the positive turbulent heat flux feedback, the positive radiative feedback in this region can significantly enhance the persistence of SST anomalies during the boreal winter. The Gulf of Mexico and nearby western Atlantic Ocean exhibit negative radiative feedback during winter and positive radiative feedback during MAM.

3) TROPICAL PACIFIC AND INDIAN OCEANS

In the vicinity of tropical deep convection regions, there is a general tendency for strong negative cloud SW feedback to cancel strong positive clear LW feed-

back. Some of the positive LW feedback are associated with cloud feedback but are much weaker than the clear-sky feedback. A similar lag-covariance analysis using precipitation data during 1979–2001 (Xie and Arkin 1997) and outgoing LW radiation (OLR) data at the top of the atmosphere during 1974–99 (Waliser and Zhou 1997) indicates that warm SST anomalies are followed by enhanced precipitation and reduced OLR in this feedback region (not shown). Thus, a simple plausible explanation for this feedback is that both cloud fraction [i.e., cirrus anvil clouds in the vicinity of updraft regime and precipitating stratiform clouds in the downdraft regime (Houze 1993)] and atmospheric water vapor increase over warm SST anomalies in association with enhanced deep convection. Both precipitating stratiform and cirrus anvil clouds are likely to reflect incoming solar radiation and thereby cool the underlying sea surface (Ramanathan and Collins 1991) while enhanced atmospheric water vapor and enhanced cirrus anvil clouds may increase downwelling LW radiation and warm the sea surface (Manabe and Strickler 1964).

Opposite feedbacks are also observed. Over the western tropical Pacific warm pool region centered at $\sim 150^\circ\text{E}$ on the equator, warm SST anomalies decrease net downwelling LW radiation (mostly clear LW) while increasing net downwelling SW radiation (mostly cloud SW) especially in MAM and JJA. Precipitation amount (OLR) in this area tends to have near-zero or weak negative (positive) correlations with the previous month's SST anomalies (not shown). Our analysis implies that warm SST anomalies in this region do not trigger deep convection directly but atmospheric dynamic forcings counteract the effects of enhanced SST anomalies. Previous studies indicate that the tropical atmospheric intraseasonal oscillation with periods of 40–50 days [also known as the Madden–Julian oscillation (MJO; Madden and Julian 1971)] has large influences on the variations of tropical deep convection (and so corresponding clouds and atmospheric water vapor) in this region (Lau and Chan 1986; Maloney and Hartmann 1998).

In spite of the strong cancellation between SW and LW feedback, net radiative feedback can be significant. Notable are strong positive radiative feedback in the Indian Ocean centered over the Bay of Bengal in JJA–SON and west of Australia in SONDJF, and strong negative radiative feedback in the central Indian Ocean in DJFMAM and the East China Sea extending to the east in JJA. Other notable features are strong positive SW feedback over the central South Pacific and the eastern tropical Pacific Oceans in SON.

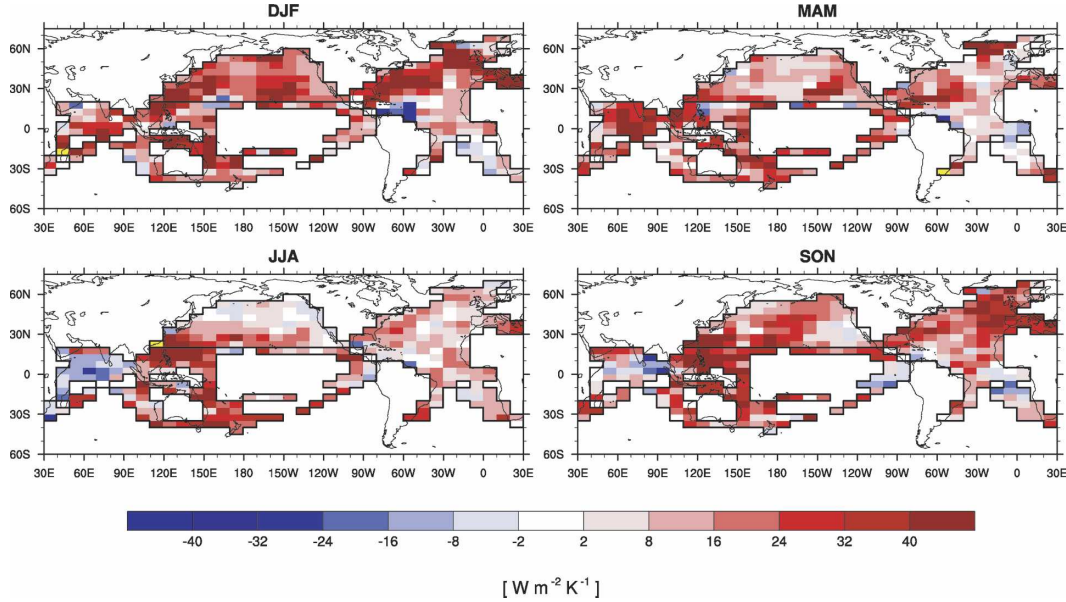


FIG. 12. Same as in Fig. 1 but for net surface heat flux feedback ($\lambda_{LHF} + \lambda_{SHF} + \lambda_{SW} + \lambda_{LW}$).

c. Net surface heat flux feedback

Figure 12 shows the sum of the turbulent and radiative heat flux feedback. Area mean values of seasonal heat flux feedback parameters are summarized in Tables 1a–c for the North Pacific (25° – 55° N, 140° E– 120° W), extratropical North Atlantic (20° – 60° N, 80° W– 0°), and tropical Atlantic Oceans (20° S– 20° N, 80° W– 10° E), respectively.

Over the North Pacific and extratropical North Atlantic Oceans, surface heat flux feedback is strongly negative during winter, with maximum values of 28 and $33 \text{ W m}^{-2} \text{ K}^{-1}$ during January for the North Pacific and extratropical North Atlantic Oceans, respectively. The annual cycle of surface heat flux feedbacks roughly follows a single sinusoidal pattern with minimum values of $5 \text{ W m}^{-2} \text{ K}^{-1}$ during June for the North Pacific and $9 \text{ W m}^{-2} \text{ K}^{-1}$ during July for the extratropical North Atlantic. Although weak, regions of positive feedback are observed over the midlatitude North Pacific during summer and over the Californian stratocumulus deck during fall. Net surface heat flux feedback over the tropical Atlantic Ocean is much weaker than the North Pacific and extratropical North Atlantic Oceans, with a maximum value of $7 \text{ W m}^{-2} \text{ K}^{-1}$ during July and a minimum value of $0 \text{ W m}^{-2} \text{ K}^{-1}$ during November. Regions of strong positive heat flux feedback occur over the tropical western North Atlantic Ocean during winter and over the Namibian stratocumulus deck during SON. Net heat flux feedback over the western tropical Pacific Ocean is negative but positive feedback occurs over the Indian Ocean during JJASON. Over the

far eastern tropical Pacific Ocean, there is a hint of net positive feedback during SON.

To obtain insights into the role of surface heat flux feedback on the evolution of SST anomalies, we divided the net heat flux feedback ($\lambda_a \equiv \lambda_{LHF} + \lambda_{SHF} + \lambda_{SW} + \lambda_{LW}$) by the heat capacity (ρC_p) multiplied by the monthly climatology of ocean mixed layer depth (H) obtained from the dataset of Monterey and Levitus (1997; Fig. 13 in per monthly units). This quantity [$\lambda_a / (\rho C_p H)$] represents the inverse of the e -folding time of SST anomalies in association with surface heat flux feedback in the stochastic climate model of Frankignoul and Hasselmann (1977), as can be seen in the following anomalous heat budget equation of ocean mixed layer:

$$\rho C_p H \frac{d}{dt} \text{SST}' = -(\lambda_a + \lambda_0) \text{SST}' + F', \quad (4)$$

where λ_0 is an oceanic feedback parameter and F' are forcings not associated with local heat flux feedback. Even though negative surface heat flux feedback is strongest during winter (Fig. 12), damping of SST anomalies associated with surface heat flux feedback in the North Pacific and extratropical North Atlantic Oceans tend to occur most rapidly during late summer and fall, with minimum SST e -folding times of 2.3 months in the North Pacific and 1.5 months in the extratropical North Atlantic (see Tables 1a,b).

One of the most interesting features is the significant enhancement of SST persistence by positive radiative feedback over the North Pacific during late spring and

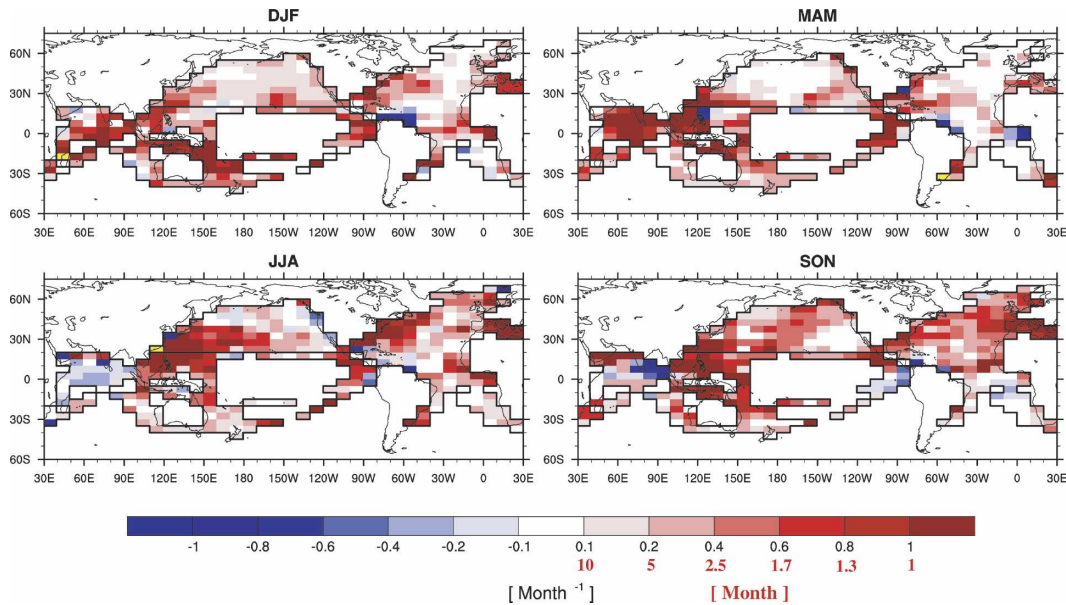


FIG. 13. Inverse of SST anomaly e -folding time associated with net surface heat flux feedback (month^{-1}) $[(\lambda_{\text{LHF}} + \lambda_{\text{SHF}} + \lambda_{\text{SW}} + \lambda_{\text{LW}})/(\rho C_p H)]$. Inverses of the values, indicated by red numerals below the color bar, represent the e -folding time of SST anomalies due to net surface heat flux feedback.

summer. Without radiative feedback, SST e -folding time associated with turbulent heat flux feedback is maximum during February (6.3 months) and minimum during August (1.8 months) over the North Pacific (Table 1a). During winter, negative radiative feedback slightly decreases the persistence of the SST anomalies. However, during later spring and early summer, positive radiative feedback significantly increases the month-to-month persistence of the SST anomalies, with a maximum increase of e -folding time during June (from 2.8 to 5.3 months) when positive radiative feedback is up to $\sim 50\%$ of negative turbulent heat flux feedback (cf. with $\sim 2\%$ during winter; see Table 1a). This result is qualitatively consistent with Zhang et al. (1998) and Norris et al. (1998) who argued that strong persistence of the leading mode of summer SST anomalies in the North Pacific is due to the positive radiative feedback associated with MBL stratiform clouds. However, we note that modulation of MBL clouds by remote ENSO forcing can also have an influence on summer SST anomaly persistence (Park and Leovy 2004; Alexander et al. 2004; Park et al. 2005, manuscript submitted to *J. Climate*).

4. Summary and discussion

Following the method described by Frankignoul and Kestenare (2002), we estimated surface heat flux feedback using 42 yr of ship-derived monthly turbulent heat

flux data and 17 yr of satellite-derived radiative flux data over the global ocean for individual seasons. To obtain insights into the mechanisms responsible for the observed surface heat flux feedback, we separately examined the responses of moisture, temperature, and wind speed of the near-surface air to the underlying SST anomalies. We also decomposed the radiative feedback into the contributions from SW and LW components, and each SW and LW feedback was further decomposed into the clear-sky and cloud components.

Over the North Pacific and extratropical North Atlantic Oceans, turbulent heat flux feedback damps SST anomalies, with maximum (minimum) negative feedback during winter (summer) when the climatological surface wind speed is strong (weak) and moistening and warming of near-surface air over warm SST anomalies is relatively weak (strong). Patches of strong negative turbulent heat flux feedback in these regions result from enhanced surface wind speed and relatively weak moisture–temperature adjustments of near-surface air over warm SST anomalies. Enhancements of MBL turbulence and incorporation of dry and fast-moving upper air into the lower MBL may be responsible for these responses. Over the western tropical Pacific and Indian Oceans, turbulent heat flux feedback is generally negative. On the other hand, positive turbulent heat flux feedback is observed over the western and central tropical Atlantic Oceans especially over the Caribbean Sea during winter. A plausible mechanism for

this is the hydrostatic reduction of SLP and the associated weakening of the Atlantic trade winds over warm SST anomalies. However, imperfect removal of nonlinear remote ENSO influences may also contribute to this positive feedback.

Positive radiative feedback over the central and eastern North Pacific Ocean during late spring through fall is due to strong positive SW feedback mainly associated with variations of MBL stratocumulus cloud fraction. Deepening and vertical decoupling of the MBL from the sea surface and associated reduction of MBL stratocumulus cloud fraction over warm SST anomalies is likely to be responsible. In the central North Pacific, weakening of synoptic storm activity and accompanying cold advection over warm SST anomalies may also contribute. Strong positive radiative feedback associated with MBL stratocumulus cloud is also observed over the southeastern subtropical Atlantic Ocean (Namibian stratocumulus deck) during SON.

Positive radiative feedback associated with the variations of clear-sky LW radiation occurs in the vicinity of deep convection regions: the western tropical North Atlantic Ocean during SONDJF and the eastern part of the Atlantic ITCZ during MAM. This is presumably due to enhanced atmospheric water vapor over warm SST anomalies. Positive clear-sky LW feedback is also observed over the western tropical Pacific and Indian Oceans with weak contributions from the cloud component, but these are significantly cancelled by negative cloud SW feedback. Increases of upper-level cirrus and low-level precipitating stratiform clouds in association with enhanced deep convection are likely to be responsible for the negative SW feedback. However, we also found the opposite effects over the western Pacific warm pool region during MAMJJA. In spite of the strong cancellation between SW and LW feedbacks, the net radiative feedback can be significant.

In summary, negative net surface heat flux feedback (i.e., damping of the underlying SST anomalies) dominates over the global oceans. However, several regions are identified with positive net heat flux feedback: the tropical western North Atlantic Ocean during DJF, the Namibian stratocumulus deck during SON, and western (eastern) Indian Ocean during JJA (SON). Over the North Pacific and extratropical North Atlantic Oceans in summer, surface heat flux feedback is weakly negative in general, although patches of positive feedback are also observed. In these regions, the negative heat flux feedback is strongest during winter but the associated SST e -folding time is shortest during late summer and fall due to the seasonal variation in ocean mixed layer depth. Our analysis indicates that positive radiative feedback associated with MBL stratocumulus

clouds can significantly enhance month-to-month persistence of the SST anomalies in the North Pacific Ocean during late spring through summer.

Our observational estimates of surface heat flux feedback can be used to assess the realism of simulated air–sea heat flux feedback in coupled ocean–atmosphere general circulation models (see Frankignoul et al. 2004). In addition, our results can provide valuable information for simple stochastic climate modeling studies aimed at simulating statistical properties of observed SST anomalies (e.g., Deser et al. 2003; Coetlogon and Frankignoul 2003). With our estimates of the radiative feedback parameters, it may be possible to quantitatively assess the contribution of MBL clouds to the persistence of extratropical SST anomalies (Park et al. 2005, manuscript submitted to *J. Climate*).

Acknowledgments. We express our thanks to Profs. Conway B. Leovy, C. Frankignoul, Joel R. Norris, and Robert Wood for valuable comments on this work. We also thank Adam Phillips for help in preparing the figures. Our thanks also go to the anonymous reviewers for their remarks, which helped to improve the draft. Sungsu Park is supported by the Advanced Study Program. Clara Deser and Michael Alexander gratefully acknowledge support from the NOAA/CLIVAR Program.

APPENDIX

Estimation of Net Downward Surface Heat Fluxes from Individual Ship Observations

Downward latent (Q_{LE} in units of watts per meters squared) and sensible (Q_{SH} in units of watts per meters squared) heat fluxes are calculated using the following bulk formula:

$$Q_{LE} = -\rho L_v C_q U (0.98 q_{so} - q_v), \quad (A1)$$

$$Q_{SH} = -\rho C_p C_h U (SST - T_a), \quad (A2)$$

where ρ is the density of surface air [$\rho = p/[R_d T_a (1 + 0.61 q_v)]$], where p is sea level pressure and R_d is gas constant of dry air ($= 287 \text{ J K}^{-1} \text{ Kg}^{-1}$); L_v is the latent heat of vaporization ($= 2.5 \times 10^6 \text{ J Kg}^{-1}$); C_p is the specific heat of surface air at constant pressure ($= 1004 \text{ J K}^{-1} \text{ Kg}^{-1}$); U is the surface wind speed; C_q and C_h are the bulk transfer coefficients of moisture and heat, respectively; q_{so} is the saturation specific humidity at SST with zero salinity; q_v is the specific humidity of surface air (kg kg^{-1}); and T_a is the surface air temperature. In Eq. (A1), 0.98 is multiplied to q_{so} by considering a reduction of saturation vapor pressure by salinity effects (Kraus 1972). It is assumed that $C_h = 0.94 C_q$ and C_q are

given as functions of U and $SST - T_a$ [see Table 4 of Isemer and Hasse (1985)]. In general, C_q is an increasing function of U and $SST - T_a$. In the above equations, U should be the wind speed at 10-m height but we simply used a ship-reported surface wind speed as U .

Net downwelling SW radiation at the sea surface (Q_{SW} in units of $W m^{-2}$) is calculated using the following empirical formula of Reed (1977):

$$Q_{SW} = Q_{SW,CLR}(1 - 6.2 \times 10^{-3}N + 0.0019\alpha), \quad (A3)$$

where $Q_{SW,CLR}$ is the net downwelling daily mean SW radiation at the sea surface for clear sky ($W m^{-2}$) as functions of latitude and time of day of the year [Eq. (1) of Reed (1977)] assuming a uniform atmospheric transmission coefficient of 0.7 over the global ocean; N is the daily mean total cloud cover (%); and α is the noon solar elevation angle ($^\circ$). Equation (A3) was derived for application to daily mean cloud cover but we applied Eq. (A3) for individual observations assuming all the ship observations are made at local noon.

Net downwelling LW radiation at the sea surface (Q_{LW} in units of $W m^{-2}$) is calculated using the following empirical formula of Budyko (1974):

$$Q_{LW} = -\delta\sigma T_a^4(0.254 - 4.95 \times 10^{-3}e) \\ (1 - 10^{-2}cN) - 4\delta\sigma T_a^3(SST - T_a), \quad (A4)$$

where δ is the emissivity ($= 0.95$); σ is the Stefan-Boltzmann constant ($= 5.6696 \times 10^{-8} W m^{-2} K^{-4}$); e is the water vapor pressure of surface air (hPa); and c is a coefficient increasing with latitude [$= 0.5 \sim 0.82$, see Table 9 on p. 59 of Budyko (1974)].

In calculation of Q_{SW} and Q_{LW} , the observations executed under poor illumination conditions are prefiltered following a screening criteria developed by Hahn et al. (1995). After calculating downward surface fluxes (Q_{LE} , Q_{SH} , Q_{SW} , Q_{LW}) using individual ship observations for the respective local daytime (0600–1800) and nighttime (1800–0600) observations, a daily average is calculated by giving the same weighting to the respective daytime and nighttime average. If either the daytime or nighttime average value is missing, the other was used as the daily average.

REFERENCES

- Alexander, M. A., and J. D. Scott, 2002: The influence of ENSO on air–sea interaction in the Atlantic. *Geophys. Res. Lett.*, **29**, 1701, doi:10.1029/2001GL014347.
- , I. Blade, M. Newman, J. R. Lanzante, N. C. Lau, and J. D. Scott, 2002: The atmospheric bridge: The influence of ENSO teleconnections on air–sea interaction over the global oceans. *J. Climate*, **15**, 2205–2231.
- , N.-C. Lau, and J. D. Scott, 2004: Broadening the atmospheric bridge paradigm: ENSO teleconnections to the North Pacific in summer and to the tropical west Pacific–Indian Oceans over the seasonal cycle. *Earth's Climate: The Ocean–Atmosphere Interaction, Geophys. Monogr.*, No. 147, Amer. Geophys. Union, 85–104.
- Barsugli, J. J., and D. S. Battisti, 1998: The basic effects of atmosphere–ocean thermal coupling on midlatitude variability. *J. Atmos. Sci.*, **55**, 477–493.
- Bretherton, C. S., and M. C. Wyant, 1997: Moisture transport, lower-tropospheric stability, and decoupling of cloud-topped boundary layers. *J. Atmos. Sci.*, **54**, 148–167.
- Budyko, M. I., 1974: *Climate and Life*. International Geophysical Series, Vol. 18, Academic Press, 508 pp.
- Chang, P., L. Ji, and R. Saravanan, 2001: A hybrid coupled model study of tropical Atlantic variability. *J. Climate*, **14**, 361–390.
- Coetlogon, G., and C. Frankignoul, 2003: The persistence of winter sea surface temperature in the North Atlantic. *J. Climate*, **16**, 1364–1377.
- Deser, C., M. A. Alexander, and M. S. Timlin, 2003: Understanding the persistence of sea surface temperature anomalies in midlatitudes. *J. Climate*, **16**, 57–72.
- Frankignoul, C., 1985: Sea surface temperature anomalies, planetary waves and air–sea feedback in the middle latitudes. *Rev. Geophys.*, **23**, 357–390.
- , and K. Hasselmann, 1977: Stochastic climate models. Part 2. Application to sea-surface temperature variability and thermocline variability. *Tellus*, **29**, 289–305.
- , and E. Kestenare, 2002: The surface heat flux feedback. Part I: Estimates from observations in the Atlantic and the North Pacific. *Climate Dyn.*, **19**, 633–647.
- , A. Czaja, and B. L'Heveder, 1998: Air–sea feedback in the North Atlantic and surface boundary conditions for ocean models. *J. Climate*, **11**, 2310–2324.
- , E. Kestenare, M. Botzet, A. F. Carril, H. Drange, A. Paradaens, L. Terray, and R. Sutton, 2004: An intercomparison between the surface heat flux feedback in five coupled models, COADS and the NCEP reanalysis. *Climate Dyn.*, **22**, 373–388.
- Hahn, C. J., and S. G. Warren, 1999: Extend edited synoptic cloud reports from ships and land stations over the globe, 1952–1996. Carbon Dioxide Information Analysis Center Rep. NDP026C, Oak Ridge National Laboratory, Oak Ridge, TN, 71 pp.
- , —, and J. London, 1995: The effect of moonlight on observation of cloud cover at night, and application to cloud climatology. *J. Climate*, **8**, 1429–1446.
- Hoerling, M. P., A. Kumar, and M. Zhong, 1997: El Niño, La Niña, and the nonlinearity of their teleconnections. *J. Climate*, **10**, 1769–1786.
- Houze, R. A., 1993: *Cloud Dynamics*. Academic Press, 573 pp.
- Isemer, H.-J., and L. Hasse, 1985: *The Bunker Climate Atlas of the North Atlantic Ocean*. Vol. 2, *Air–Sea Interactions*, Springer-Verlag, 252 pp.
- Kaplan, A., M. A. Cane, Y. Kushnir, A. C. Clement, M. B. Blumenthal, and B. Rajagopalan, 1998: Analyses of global sea surface temperature 1856–1991. *J. Geophys. Res.*, **103**, 18 567–18 590.
- Klein, S. A., 1997: Synoptic variability of low-cloud properties and meteorological parameters in the subtropical trade wind boundary layer. *J. Climate*, **10**, 2018–2039.
- , B. J. Soden, and N. C. Lau, 1999: Remote sea surface temperature variations during ENSO: Evidence for a tropical atmospheric bridge. *J. Climate*, **12**, 917–932.

- Kraus, E. B., 1972: *Atmosphere–Ocean Interaction*. Oxford University Press, 275 pp.
- Lau, K. M., and P. H. Chan, 1986: Aspects of the 40–50 day oscillation during the northern summer as inferred from outgoing longwave radiation. *Mon. Wea. Rev.*, **114**, 1354–1367.
- Lau, N. C., and M. J. Nath, 1996: The role of the “atmospheric bridge” in linking tropical Pacific ENSO events to extratropical SST anomalies. *J. Climate*, **9**, 2036–2057.
- Madden, R. A., and P. R. Julian, 1971: Detection of a 40–50 day oscillation in the zonal wind in the tropical Pacific. *J. Atmos. Sci.*, **28**, 702–708.
- Maloney, E. D., and D. L. Hartmann, 1998: Frictional moisture convergence in a composite life cycle of the Madden–Julian oscillation. *J. Climate*, **11**, 2387–2403.
- Manabe, S., and R. F. Strickler, 1964: Thermal equilibrium of the atmosphere with a convective adjustment. *J. Atmos. Sci.*, **21**, 361–385.
- Monterey, G. I., and S. Levitus, 1997: *Climatological Cycle of Mixed Layer Depth in the World Ocean*. NOAA/NESDIS, 5 pp. and 87 figs.
- Nonaka, M., and S. P. Xie, 2003: Covariations of sea surface temperature and wind over the Kuroshio and its extension: Evidence for ocean-to-atmosphere feedback. *J. Climate*, **16**, 1404–1413.
- Norris, J. R., 1998a: Low cloud type over the ocean from surface observations. Part I: Relationship to surface meteorology and the vertical distribution of temperature and moisture. *J. Climate*, **11**, 369–382.
- , 1998b: Low cloud type over the ocean from surface observations. Part II: Geographical and seasonal variations. *J. Climate*, **11**, 383–403.
- , 2000: Interannual and interdecadal variability in the storm track, cloudiness, and sea surface temperature over the summertime North Pacific. *J. Climate*, **13**, 422–430.
- , and C. B. Leovy, 1994: Interannual variability in stratiform cloudiness and sea surface temperature. *J. Climate*, **7**, 1915–1925.
- , Y. Zhang, and J. M. Wallace, 1998: Role of low clouds in summertime atmosphere–ocean interactions over the North Pacific. *J. Climate*, **11**, 2482–2490.
- North, G. R., T. L. Bell, R. F. Cahalan, and F. J. Moeng, 1982: Sampling errors in the estimation of empirical orthogonal functions. *Mon. Wea. Rev.*, **110**, 699–706.
- Park, S., 2004: Remote ENSO influence on Mediterranean sky conditions during late summer and autumn: Evidence for a slowly evolving atmospheric bridge. *Quart. J. Roy. Meteor. Soc.*, **130**, 2409–2422.
- , and C. B. Leovy, 2004: Marine low cloud anomalies associated with ENSO. *J. Climate*, **17**, 3448–3469.
- , —, and M. A. Rozendaal, 2004: A new heuristic Lagrangian marine boundary layer cloud model. *J. Atmos. Sci.*, **61**, 3002–3024.
- Ramanathan, V., and W. Collins, 1991: Thermodynamic regulation of ocean warming by cirrus clouds deduced from observations of the 1987 El Niño. *Nature*, **351**, 27–32.
- Reed, R. K., 1977: On estimating insolation over the ocean. *J. Phys. Oceanogr.*, **7**, 482–485.
- Rossow, W. B., and R. A. Schiffer, 1991: ISCCP cloud data products. *Bull. Amer. Meteor. Soc.*, **72**, 2–20.
- Saravanan, R., and P. Chang, 2000: Interaction between tropical Atlantic variability and El Niño–Southern Oscillation. *J. Climate*, **13**, 2177–2194.
- Waliser, D. E., and W. Zhou, 1997: Removing satellite equatorial time biases from the OLR and HRC datasets. *J. Climate*, **10**, 2125–2146.
- Wang, C., and D. B. Enfield, 2003: A further study of the tropical Western Hemisphere warm pool. *J. Climate*, **16**, 1476–1493.
- Woodruff, S. D., R. J. Slutz, R. L. Jenne, and P. M. Steurer, 1987: A Comprehensive Ocean–Atmosphere Data Set. *Bull. Amer. Meteor. Soc.*, **68**, 1239–1250.
- Xie, P., and P. A. Arkin, 1997: Global precipitation: A 17-year monthly analysis based on gauge observations, satellite estimates, and numerical model outputs. *Bull. Amer. Meteor. Soc.*, **78**, 2539–2558.
- Zhang, Y., J. R. Norris, and J. M. Wallace, 1998: Seasonality of large-scale atmosphere–ocean interaction over the North Pacific. *J. Climate*, **11**, 2473–2481.
- Zhang, Y. C., and W. B. Rossow, cited 2004: New ISCCP global radiative flux data products. [Available online at <http://isccp.giss.nasa.gov/projects/flux.html>.]